# Accounting for Sample Morphology in Correlative X-Ray Microscopy via Ray Tracing

Rishi E. Kumar, Xueying L. Quinn, David P. Fenning
Materials Science and Engineering
University of California, San Diego

## Abstract

The correlations in multi-modal microscopy data can be systematically reduced by the distinct probe-sample interactions and signal collection geometry for each modality. Extracting scientific insights from correlative datasets thus requires careful consideration of the mode-specific, and often non-overlapping, sampling volume used in the correlative microscopy. Here we describe a pencil-beam, ray-tracing method that accounts for the finite extent and roughness of thin films and nanomaterials in synchrotron-based X-ray microscopy measurements, creating a first approximation of the probe-sample interaction for each modality that tightens correlations in multi-modal X-ray nanoprobe characterization. As a demonstrative example we analyze structure-function correlations in sequential microscopy data acquired for a Eu:$CsPbBr_3$ halide perovskite thin film crystal across three distinct measurement modes. Our ray-traced corrections account for local fluorescence matrix effects and sampling volume discrepancies and unveil structural, compositional, and optoelectronic relationships hidden in the raw data.

## 1. Introduction

Drawing correlations such as structure-property relationships is integral to the study of materials. To this end, studies that combine spatially-resolved characterization by multiple modalities can offer strong explanatory power, correlating physical or functional properties at the local level. In particular, the growth in capabilities of and access to synchrotron facilities around the world has enabled novel multi-modal studies on materials ranging from biological samples[1–3] to next-generation photovoltaic materials.[4–10] Extracting scientific insights from these correlative datasets requires careful consideration of the mode-specific, and often non-overlapping, sampling volume used in the correlative microscopy. Here we describe a ray-tracing method that accounts for the finite extent and roughness of thin films and nanomaterials, creating a first approximation of the probe-sample interaction for each modality that tightens correlations in multi-modal nanoprobe characterization.

The correlations in multimodal microscopy data, *e.g.* generated by synchrotrons, can be systematically reduced by geometric factors and local probe-sample interactions. For example, matrix effects can alter X-ray fluorescence (XRF) measurements, where the path length of both incident and fluoresced photons within the sample can selectively attenuate a given element's signal recorded at the detector [11–13]. Geometric factors can be significant in the study of samples anisotropic in either morphology or composition, such as porous battery electrodes[14, 15], catalysts [16, 17], standalone single-crystals [5], biological cells [18], or patterned semiconductor devices[19]. Furthermore, these factors compound when relating multiple measurements of a sample. Whether acquired in a synchronous correlative microscopy approach or via sequential measurements, each mode of data is subject to unique geometric effects determined by instrument geometry and sample properties.

A variety of modeling tools are available for simulating the beam propagation to the sample plane in synchrotron experiments built on top of ray-tracing solvers, of which SHADOW (currently SHADOW3) is most widely used.[20]–[21, 22] Though these tools give an accurate estimate of the beam profile at the sample plane, a critical missing component for the experimentalist is simulating the propagation of this beam through a heterogeneous sample and subsequent signal generation. No available tools to our knowledge address the issue of spatially-variant probe-sample interactions.

To address this challenge, we present a morphology-informed ray tracing approach to simulate probe-sample interactions in raster scanning measurements, allowing for a first approximation of matrix effects and spatial correlation of the data acquired across scanning synchrotron-based and optical microscopy setups. As a demonstrative example we analyze structure-function correlations in sequential microscopy data acquired for a Eu:$CsPbBr_3$ halide perovskite thin film crystal [23] in three distinct measurement modes, each with its own measurement geometry: nanoprobe X-ray diffraction (nXRD), nanoprobe X-ray fluorescence (nXRF), and normal-incidence confocal micro-photoluminescence (µPL) [5]. First, we establish a three-dimensional (3D) model of our sample with nanoscopic accuracy using 3D optical profilometry. Next, each measurement geometry is defined for simulation by the orientation of the incident photon probe, sample, and involved detectors. We then perform ray tracing of the X-ray beam propagation within our sample, accounting for attenuation of incident and detected photons within the sample. Ray tracing generates a "sample point-spread function" (sPSF) that encodes the weighted contribution of sample volume to the signal recorded at the detector during each mode of measurement (*i.e.,* scattering and fluorescence). By accounting for local geometric effects in our measurements, we correct the nXRF and nXRD data for attenuation and improve the precision of the spatial correlation across our three modalities. Such precise assessment of sampling volume and matrix effects in correlative measurements will be increasingly necessary as the volume and complexity of multimodal studies increases at upgraded and next-generation synchrotron facilities.

## 2. Methods

### *2.1 Synchrotron X-Ray Fluorescence and X-Ray Diffraction:*

Nano-XRF and nano-XRD were both acquired at the 26-ID-C beamline at the Center for Nanoscale Materials and the Advanced Photon Source at Argonne National Laboratory, using a focused 10 keV x-ray beam (beam waist <200 nm). Fluorescence maps (500 nm step size) were acquired with the sample oriented such that the sample substrate normal is 20° off the incident beam axis. The fluorescence detector, oriented 90° off the incident beam axis, was calibrated using NIST XRF standards (NBS1832, NBS1833). Local d-spacing of the (066) plane was determined by performing a spatially-resolved rocking curve (500 nm step size) in the Bragg condition, where the incident and detector angles were held constant while the sample theta was rotated in 0.25° increments. The 2D scattering detector was calibrated by measurement of a powder silicon reference sample. This procedure enables complete reconstruction of the 3D scattering vector at each point.

### *2.2 Defining the Simulation Volume*

The topography of the crystals was measured with a Filmetrics Profilm3D in White Light Interferometry mode with 50x magnification at lateral resolution of 100 nm and a vertical resolution of 0.1 nm. We construct a 3D model of our sample from this profilometry data (Figure S1, detailed procedure given in the Supporting Information). The instrument geometry is defined by the Euler angles of the incident beam and the detector axis with respect to the sample. Our synchrotron measurements utilize a nanoprobe with a beam waist of <200 nm. As such, we treat both the incident probe and signal photons as pencil beams propagating in the directions defined by the Euler angles.

The simulation mesh is generated by interpolation of the sample model onto a mesh scaled to match the highest resolution dimension (in our case, the $z$-dimension), generating more points along the coarse lateral dimensions. The mesh is then extended in the $xy$-plane to accommodate the lateral projection of the incident beam trajectory.

### *2.3 Ray Tracing*

For each lateral coordinate $(x, y)$, a single ray is simulated starting from the top of the simulation mesh $(x, y, z_{max})$. As this ray propagates along the incident direction with a step size $d_{step}$, two events occur for each step where the ray intersects the sample: the intersection is recorded, and a signal ray is spawned. The signal ray similarly propagates towards the detector until $z = z_{max}$, and the total number of steps where the sample is intersected is recorded. A schematic of one ray simulation is shown in Figure 1g. The full algorithm is detailed in the Supporting Information.

### *2.4 Estimating Self Absorption*

We approximate the X-ray attenuation coefficient μ within our sample for relevant photon energies by the material's density and nominal average elemental composition.[24] The attenuation coefficient is applied to the intersection points tabulated during ray tracing, with each incident ray starting with unit intensity and each signal ray starting with the intensity lost from the incident beam in one step (Algorithm 3 in Supplemental Information). The fraction of the "true" fluorescence signal as measured for each lateral coordinate is taken to be the sum of all final signal ray intensities at that coordinate. Measured fluorescence values are then divided by this fraction to remove self-absorption effects. By separating the expensive ray tracing from the attenuation calculations for each element's signal, we quickly apply the ray tracing results to fluorescence data for elements with different emission energies.

## 3. Results and Discussion

### *3.1 Correcting Fluorescence Data for Self-Absorption*

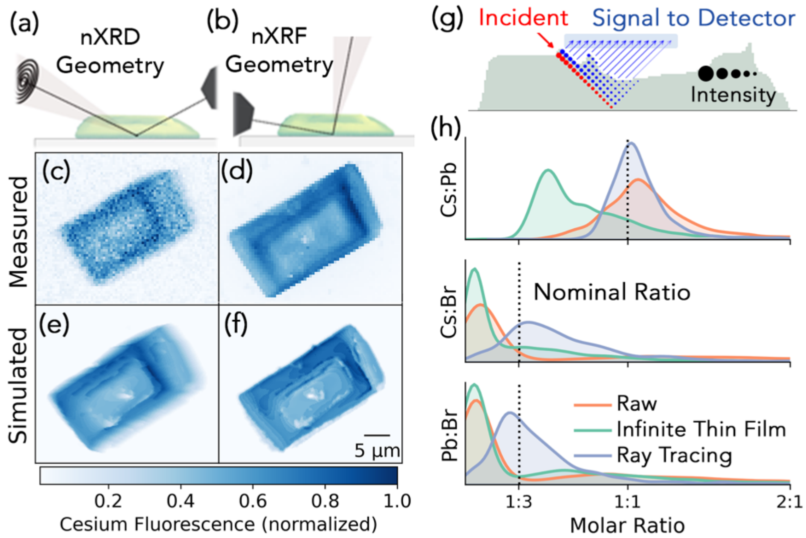

Figure 1: Instrument geometries where nano X-ray fluorescence was collected: (a) a correlative Bragg scattering configuration (a) and a geometry optimized for only nano X-ray fluorescence signal, with respective simulated (c,d) and measured (e,f) cesium fluorescence maps of the Eu:CsPbBr3 thin film crystal. (g) Single-ray example of the ray tracing process showing the incident ray and all collected signal rays. (h) Distribution of raw, thin-film corrected[13], and ray-trace corrected molar ratios measured in the fluorescence-optimized geometry. The dashed vertical line shows the nominal composition ratio.

We first validate our ray tracing approach by comparing simulated and measured X-ray fluorescence signals acquired in two different sampling geometries. Simulated and measured cesium XRF data collected from the same Eu:$CsPbBr_3$ sample in Bragg nXRD and nXRF geometries are shown in Figure 1a-f. Cesium XRF intensity is simulated by assuming that the cesium concentration is constant across the volume of the microcrystal, a fair assumption in our largely-single-crystalline sample.[5, 23] The simulations capture the crystal's hopper morphology[25] and, especially, the horizontal smearing by the beam projection in the shallow Bragg geometry (Figure 1c,e). Sharper contrast in the simulated maps can be attributed to our pencil beam assumption. This would be reduced by expanding the ray tracing model to account for the angular distribution of incident photons defined by the zone plate numerical aperture, finite tails of the probe shape, and the solid angle of collection of the detectors.

Ray tracing the incident and emitted photons in the X-ray fluorescence measurement enables correction for self-absorption.[26, 27] The degree to which the raw fluorescence data is affected by self-absorption depends on the sample composition and the path length of photons within the sample (Figure S3). West *et al.* formalized an effective process for self-absorption correction in planar thin-film samples, where these path lengths are well defined.[13] The geometric assumptions made in their process do not apply to our rough, anisotropic crystal. By raytracing, we extend the analysis of West *et al*., accounting for varying path lengths across the sample. The molar ratios of the major components in our perovskite microcrystal converge to the expected stoichiometry after correction by our ray tracing approach (Figure 1g). The distribution tails are also reduced, as lateral variations in self-absorption (from the position of the fluorescence detector to the left of the sample) are corrected. We note that our quantification of bromine content is made using the $Br_{L\alpha}$ line, the low signal of which contributes to broad distributions of molar ratios involving bromine.

### *3.2 Accounting for Geometric Differences via Convolution*

Ray tracing returns not only the relative signal measured for each pixel in our spatial dataset, but the points in the sample from which that signal is generated. The ray-tracing simulation assembles a rank five tensor where each coordinate $(x, y)$ holds the local sample point-spread function $sPSF(x, y, z)$, a sparse 3D mask encoding the weighted contribution of each point in the sample to the total signal recorded at the detector for coordinate $(x, y)$. As the nXRF, nXRD, and μ-PL data are sampled only in the two lateral dimensions in the plane of the thin film crystal (all signal generated in the dept of the sample is projected into 2D), we integrate the sPSF along the Z-direction. Examples of local sPSF's from the nXRD geometry are shown in Figure S2. In our case, we measured our perovskite crystal sequentially in three mapping measurements: nXRD, nXRF, and μPL. sPSFs were determined for the nXRD and nXRF geometries. The μPL sPSF sPSF was set to the identity matrix, as the optical path of the confocal microscope used is normal to the sample and incurs no lateral projection.

We can use the resulting rank four tensor, which describes local 2D convolution, to better analyze the correlations between our 2D mapping data from different modalities. Even perfectly registered maps encode information from different sample volumes owing to the geometry differences and the differing light-matter interactions at hand with the change in photon energies. The raytraced sPSF enables a more precise comparison across multiple measurements with varied interaction volumes.

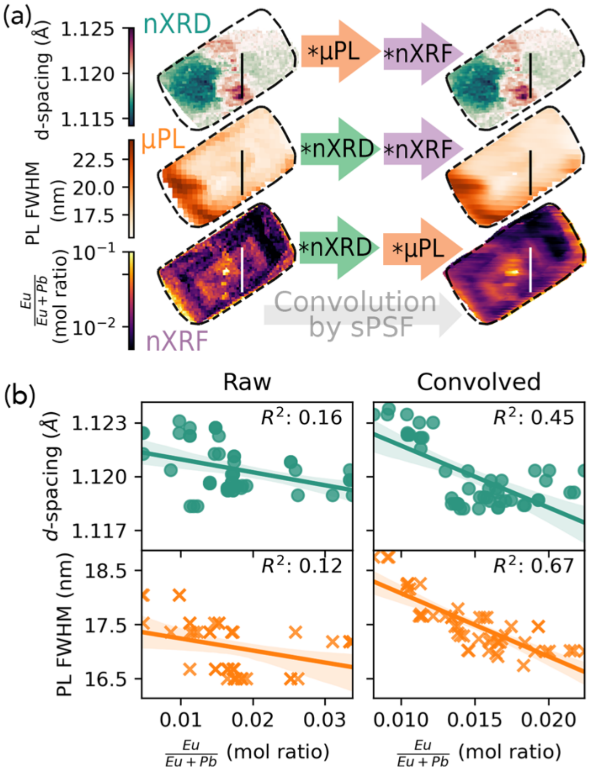

Figure 2: (a) Convolution of each of the nano X-ray diffraction (nXRD), micro photoluminescence (μPL), and nano X-ray fluorescence (nXRF) data by the sample point-spread functions (sPSF) from the other data geometries yields equivalently convolved images. (b) Pixelwise correlation of the *d*-spacing from nXRD and

the μPL full-width half-maximum (FWHM) with the local europium content from nXRF along the vertical lines in (a). Linear fits (solid lines) and associated R-squared values are shown for each correlation both before (left) and after (right) convolution. The shading represents 95% prediction intervals.

All raw measured data can be thought of as a convolution of the true sample nature by the sPSF. Deconvolution of the sPSF from the raw data would recover the map of the sample properties at the highest sampling resolution. In practice, the noise level of experimental data prohibits a deconvolution approach. This issue is further exacerbated by the spatially-variant nature of our PSF. Existing algorithms for spatially-variant deconvolution hinge on finding sections with multiple constant-PSF chunks, whether by recovering the image in sections with constant PSFs and stitching or by decomposing the spatially-variant PSF into eigenfunctions and continuously varying their eigenvalues across the image area [28–32]. These methods may be applicable for samples with periodic features and thus a small number of unique local PSFs, but for general cases these algorithms may not suffice.

A simpler (albeit less satisfying) approach to reconcile sampling volume differences across datasets is to convolve each dataset by the sPSF of the others (Figure 2a). Though the spatial resolution of each individual image is reduced, the total data is now equivalently convolved and can be compared pixelwise. Applied to our nXRF, nXRD, and μPL datasets, this forward convolution treatment reveals local correlation of composition, microstructure, and optoelectronic quality across a microstrain gradient observed in the nXRD (Figure 2b). Note that, applied to 2D data like ours, the sample information is implicitly compressed into the two lateral dimensions despite rays being traced in three dimensions. This shortcoming continues to wane as advanced techniques and dedicated hardware capable of resolving material structure [33–40] and composition [1, 18, 41–47] in three dimensions proliferate across upgraded synchrotron facilities. These 3D techniques also carry unique interaction volumes that must be considered in comparison across modalities, for which our approach can be employed to mutually convolve the data modalities in 3D. Still, these techniques are not always feasible as they require specific hardware, often incur large photon doses that prohibit sensitive samples, and, in the case of tomography, may be difficult to apply to extended thin samples such as ours. [48, 49] Regardless of the raw data dimensionality, the forward-convolution approach allows for a morphologically informed comparison across modalities.

### *3.2 Caveats and Further Considerations*

Our ray tracing approach does not take any secondary photon interactions into account. The validity of this simplification depends on the sample under study. For large, highly crystalline samples measured in a Bragg condition, dynamical scattering may significantly alter the transmission of x-rays through the sample. [24, 50] Samples of high-Z compositions may also be subject to secondary fluorescence. [51, 52] Each of these phenomena will modify the sPSF and the resulting convolutions of the data.

Self-absorption correction adjusts estimates of local composition, which in turn adjusts the expected degree of self-absorption. This suggests that an iterative solver with alternating updates to the composition and self-absorption factors could be employed to converge towards the true local composition. In our specific case this approach is not required. We have high confidence that in our high-quality crystalline sample (not a polycrystal), the local content of all elements other than lead and europium (the dopant species) are constant, and self-absorption differences between compositions at the extreme ends of our measured Pb and Eu stoichiometry only generate a 1-4% difference in our molar ratios of interest (Figure S4). Development of iterative composition solvers will be important for the study of samples with poorly constrained composition, especially in dense correlative datasets as generated in diffraction-limited and/or tomographic experiments at next-generation synchrotron facilities.

## 4. Conclusion

To realize the full power of multimodal correlative microscopy studies, the nuances of each individual mode must be accounted for. Even in a simultaneous measurement with multiple detectors, the data acquired at each detector is subject to different geometric effects within the sample. We have shown that even a simple ray-tracing approach employing pencil beams and Beer-Lambert attenuation can correct for self-absorption effects in X-ray fluorescence measurements, allowing quantitative compositions to be extracted from highly anisotropic samples. Ray tracing also generates a sample point-spread function encoding the local probe-sample interaction volume for each pixel in spatially-resolved mapping or imaging measurements, which can be used to reconcile the sampling volume differences across datasets. We show that jointly convolving the multimodal datasets with the sample point-spread function of each is a simple yet effective way of bringing spatial data into the same frame for comparison. Future development in flexible and noise-tolerant deconvolution algorithms, especially recent efforts leveraging machine learning[53–55], may make deconvolution more tractable. The ray-tracing approach described here can be improved in many ways, such as accounting for the shape and angular range of the incident probe, the collection angle of the detector, and second-order effects in modeling probe-sample interaction (*e.g.* secondary fluorescence). We envision future tools for rigorous simulation of probe-sample interactions to be built on standard ray-tracing engines like SHADOW [21, 22] and incorporated into simulation platforms like OASYS [20] to enable end-to-end simulation of multi-modal experiments from probe to detector that maximizes the ability to make scientific inference from correlative microscopy data. The promising results from our preliminary efforts prove that these tools will bring practical benefits to multimodal studies, particularly when techniques involve long path lengths such as in X-ray and neutron experiments.

## 5. Acknowledgements

Thank you to Moses Kodur at UC San Diego for his help in taking the μPL data, and to Tao Zhou, Martin V. Holt, and Zhonghou Cai from the Center for Nanoscale Materials at Argonne National Laboratory for their assistance during and valuable discussion about our synchrotron measurements. This work was supported in part by the National Science Foundation under Grant No. DMR-1848371. Use of the Center for Nanoscale Materials and the Advanced Photon Source, both Office of Science user facilities, was supported by the U.S. Department of Energy, Office of Science, Office of Basic Energy Sciences, under Contract No. DE-AC02-06CH11357. This work was performed in part at the San Diego Nanotechnology Infrastructure (SDNI) of UCSD, a member of the National Nanotechnology Coordinated Infrastructure, which was supported by the National Science Foundation (grant ECCS-1542148).

## 6. Conflict of Interest

On behalf of all authors, the corresponding author states that there is no conflict of interest.

## 7. Data Availability Statement

The datasets generated during and/or analyzed during the current study are available from the corresponding author on reasonable request.

## References

[1] M. Kreuzer, S. Stamenković, S. Chen, P. Andjus and T. Dučić, “Lipids status and copper in a single astrocyte of the rat model for amyotrophic lateral sclerosis: Correlative synchrotron-based X-ray and infrared imaging.,” *J Biophotonics*, vol. 13, no. 10, pp. e202000069, 2020

[2] B. De Samber, R. Evens, K. De Schamphelaere, G. Silversmit, B. Masschaele, T. Schoonjans, B. Vekemans, C. R. Janssen, L. Van Hoorebeke, I. Szalóki, F. Vanhaecke, G. Falkenberg and L. Vincze, “A combination of synchrotron and laboratory X-ray techniques for studying tissue-specific trace level metal distributions in Daphnia magna,” *Journal of Analytical Atomic Spectrometry*, vol. 23, no. 6, pp. 829, 2008

[3] A. Conti, R. Sinibaldi, S. Capuani, T. Traini, G. L. Romani and S. Della Penna, “Co-registration of Synchrotron Radiation-microCT and micro-MRI images: a new method for the complete characterization of newly-formed bone,” vol. Proc. Intl. Soc. Mag. Reson. Med 22, pp. 1176, 2014

[4] Y. Luo, N. Li, Z. Chen, X. Niu, R. E. Kumar, J. Jiang, H. Liu, O. Chen, B. Lai and G. Brocks, “The Impacts and Origins of A-site Instability in Formamidinium-Cesium Lead Iodide Perovskite Solar Cells Under Extended Operation,” vol. 2020 47th IEEE Photovoltaic Specialists Conference, no. PVSC, pp. 0626-0628, 2020

[5] X. L. Quinn, R. E. Kumar, M. Kodur, D. N. Cakan, Z. Cai, T. Zhou, M. V. Holt and D. P. Fenning, "Europium Addition Reduces Local Structural Disorder and Enhances Photoluminescent Yield in Perovskite CsPbBr 3," *Adv. Optical Mater.*, pp. 2002221, 2021

[6] M. Kodur, R. E. Kumar, Y. Luo, D. N. Cakan, X. Li, M. Stuckelberger and D. P. Fenning, "X-Ray Microscopy of Halide Perovskites: Techniques, Applications, and Prospects," *Advanced Energy Materials*, vol. 10, no. 26, pp. 1-25, 2020

[7] Y. Luo, S. Aharon, M. Stuckelberger, E. Magaña, B. Lai, M. I. Bertoni, L. Etgar and D. P. Fenning, "The Relationship between Chemical Flexibility and Nanoscale Charge Collection in Hybrid Halide Perovskites," *Advanced Functional Materials*, vol. 28, no. 18, pp. 1706995, 2018

[8] B. M. West, M. Stuckelberger, H. Guthrey, L. Chen, B. Lai, J. Maser, V. Rose, W. Shafarman, M. Al-Jassim and M. I. Bertoni, "Grain engineering: How nanoscale inhomogeneities can control charge collection in solar cells," *Nano Energy*, vol. 32, pp. 488-493, 2017

[9] M. Stuckelberger, B. West, T. Nietzold, B. Lai, J. M. Maser, V. Rose and M. I. Bertoni, "Engineering solar cells based on correlative X-ray microscopy," *Journal of Materials Research*, vol. 32, no. 10, pp. 1825-1854, 2017

[10] Y. Zhou, H. Zhou, J. Deng, W. Cha and Z. Cai, "Decisive Structural and Functional Characterization of Halide Perovskites with Synchrotron," *Matter*, vol. 2, pp. 360-377, 2020

[11] B. Beckhoff, B. Kanngießer, N. Langhoff, R. Wedell and H. Wolff, "Handbook of Practical X-Ray Fluorescence Analysis," Springer Science & Business Media, 2007.

[12] P. Pfalzer, J. P. Urbach, M. Klemm, S. Horn, M. L. Den Boer, A. I. Frenkel and J. P. Kirkland, "Elimination of self-absorption in fluorescence hard-x-ray absorption spectra," *Physical Review B - Condensed Matter and Materials Physics*, vol. 60, no. 13, pp. 9335-9339, 1999

[13] B. M. West, M. Stuckelberger, A. Jeffries, S. Gangam, B. Lai, B. Stripe, J. Maser, V. Rose, S. Vogt, M. I. Bertoni, IUCr, J. Maser, V. Rose, S. Vogt, M. I. Bertoni, IUCr, J. Maser, V. Rose, S. Vogt and M. I. Bertoni, "X-ray fluorescence at nanoscale resolution for multicomponent layered structures: A solar cell case study," *Journal of Synchrotron Radiation*, vol. 24, no. 1, pp. 288-295, 2017

[14] S.-M. Bak, Z. Shadike, R. Lin, X. Yu and X.-Q. Yang, "In situ/operando synchrotron-based X-ray techniques for lithium-ion battery research," *NPG Asia Materials*, vol. 10, no. 7, pp. 563-580, 2018

[15] D. A. Shapiro, Y.-s. S. Yu, T. Tyliszczak, J. Cabana, R. Celestre, W. Chao, K. Kaznatcheev, A. L. D. D. Kilcoyne, F. Maia, S. Marchesini, Y. S. Meng, T. Warwick, L. L. Yang and H. A. Padmore, "Chemical composition mapping with nanometre resolution by soft X-ray microscopy," *Nature Photonics*, vol. 8, no. 10, pp. 765-769, 2014

[16] F. Meirer and B. M. Weckhuysen, "Spatial and temporal exploration of heterogeneous catalysts with synchrotron radiation," *Nature Reviews Materials*, vol. 3, no. 9, pp. 324-340, 2018

[17] J. Becher, T. L. Sheppard, Y. Fam, S. Baier, W. Wang, D. Wang, S. Kulkarni, T. F. Keller, M. Lyubomirskiy, D. Brueckner, M. Kahnt, A. Schropp, C. G. Schroer and J.-D. Grunwaldt, "Mapping the Pore Architecture of Structured Catalyst Monoliths from Nanometer to Centimeter Scale with Electron and X-ray Tomographies," *The Journal of Physical Chemistry C*, vol. 123, no. 41, pp. 25197-25208, 2019

[18] J. Deng, Y. H. Lo, M. Gallagher-Jones, S. Chen, A. Pryor, Q. Jin, Y. P. Hong, Y. S. G. Nashed, S. Vogt, J. Miao and C. Jacobsen, "Correlative 3D x-ray fluorescence and ptychographic tomography of frozen-hydrated green algae," *Science Advances*, vol. 4, no. 11, pp. 1-11, 2018

[19] J. Bruley, M. J. Highland, S. O. Hruszkewycz, I. McNulty, C. E. Murray, M. V. Holt, A. Tripathi, P. H. Fuoss, O. G. Shpyrko, J. Holt, C. E. Murray, J. Bruley, J. Holt, A. Tripathi, O. G. Shpyrko, I. McNulty, M. J. Highland, P. H. Fuoss, S. O. Hruszkewycz, I. McNulty, C. E. Murray, M. V. Holt, A. Tripathi, P. H. Fuoss, O. G. Shpyrko, J. Holt, C. E. Murray, J. Bruley, J. Holt, A. Tripathi, O. G. Shpyrko, I. McNulty, M. J. Highland and P. H. Fuoss, "Quantitative nanoscale imaging of lattice distortions in epitaxial semiconductor heterostructures using nanofocused X-ray Bragg projection ptychography," *Nano Letters*, vol. 12, no. 10, pp. 5148-5154, 2012

[20] M. S. D. Rio and L. Rebuffi, "OASYS: A software for beamline simulations and synchrotron virtual experiments," 2019

[21] B. Lai and F. Cerrina, "SHADOW: A synchrotron radiation ray tracing program," *Nuclear Instruments and Methods in Physics Research Section A: Accelerators, Spectrometers, Detectors and Associated Equipment*, vol. 246, no. 1-3, pp. 337-341, 1986

[22] M. S. del Rio, N. Canestrari, F. Jiang and F. Cerrina, "SHADOW3: a new version of the synchrotron X-ray optics modelling package.," *J Synchrotron Radiat*, vol. 18, no. Pt 5, pp. 708-716, 2011

[23] P. Khoram, S. Brittman, W. I. Dzik, J. N. H. Reek and E. C. Garnett, "Growth and Characterization of PDMS-Stamped Halide Perovskite Single Microcrystals," *Journal of Physical Chemistry C*, vol. 120, no. 12, pp. 6475-6481, 2016

[24] B. L. Henke, E. M. Gullikson and J. C. Davis, “X-ray interactions: photoabsorption, scattering, transmission, and reflection at E= 50-30,000 eV, Z= 1-92,” *Atomic data and nuclear data tables*, vol. 54, no. 2, pp. 181-342, 1993
[25] D. Pettit and P. Fontana, “Comparison of sodium chloride hopper cubes grown under microgravity and terrestrial conditions.,” *NPJ Microgravity*, vol. 5, pp. 25, 2019
[26] A. Kuczumow, Z. Rzączyńska and M. Szewczak, “Matrix effects in the x-ray fluorescence method,” *X-Ray Spectrometry*, vol. 11, no. 3, pp. 135-139, 1982
[27] M. Franzini, L. Leoni and M. Saitta, “A simple method to evaluate the matrix effects in X-ray fluorescence analysis,” *X-ray Spectrometry*, vol. 1, no. 4, pp. 151-154, 1972
[28] J. G. Nagy and D. P. O’Leary, “Restoring images degraded by spatially variant blur,” *SIAM Journal on Scientific Computing*, vol. 19, no. 4, pp. 1063-1082, 1998
[29] K. Novak and A. T. Watnik, “Imaging through deconvolution with a spatially variant point spread function,” *Computational Imaging VI*, 2021
[30] A. Shajkofci and M. Liebling, “Semi-blind spatially-variant deconvolution in optical microscopy with local point spread function estimation by use of convolutional neural networks,” vol. 2018 25th IEEE International Conference on Image Processing, no. ICIP, pp. 3818-3822, 2018
[31] É. Thiébaut, L. Denis, F. Soulez and R. Mourya, “Spatially variant PSF modeling and image deblurring,” *Adaptive Optics Systems V*, 2016
[32] T. R. Lauer, “Deconvolution with a spatially-variant PSF,” *Astronomical Data Analysis II*, vol. 4847, no. 520, pp. 167, 2002
[33] X. Chen, C. Dejoie, T. Jiang, C.-S. Ku and N. Tamura, “Quantitative microstructural imaging by scanning Laue x-ray micro- and nanodiffraction,” *MRS Bulletin*, vol. 41, no. 6, pp. 445-453, 2016
[34] T. W. Cornelius and O. Thomas, “Progress of in situ synchrotron X-ray diffraction studies on the mechanical behavior of materials at small scales,” *Progress in Materials Science*, vol. 94, pp. 384-434, 2018
[35] F. Hofmann, R. J. Harder, W. Liu, Y. Liu, I. K. Robinson and Y. Zayachuk, “Glancing-incidence focussed ion beam milling: A coherent X-ray diffraction study of 3D nano-scale lattice strains and crystal defects,” *Acta Materialia*, vol. 154, pp. 113-123, 2018
[36] G. E. Ice, B. C. Larson, J. Z. Tischler, W. Liu and W. Yang, “X-ray microbeam measurements of subgrain stress distributions in polycrystalline materials,” *Materials Science and Engineering: A*, vol. 399, no. 1-2, pp. 43-48, 2005
[37] H. F. Poulsen, X. Fu, E. Knudsen, E. M. Lauridsen, L. Margulies and S. Schmidt, “3DXRD – Mapping Grains and Their Dynamics in 3 Dimensions,” *Materials Science Forum*, vol. 467-470, pp. 1363-1372, 2004
[38] H. Simons, A. C. Jakobsen, S. R. Ahl, C. Detlefs and H. F. Poulsen, “Multiscale 3D characterization with dark-field x-ray microscopy,” *MRS Bulletin*, vol. 41, no. 6, pp. 454-459, 2016
[39] T. Tian, R. Morusupalli, H. Shin, H.-Y. Son, K.-Y. Byun, Y.-C. Joo, R. Caramto, L. Smith, Y.-L. Shen, M. Kunz, N. Tamura and A. S. Budiman, “On the Mechanical Stresses of Cu Through-Silicon Via (TSV) Samples Fabricated by SK Hynix vs. SEMATECH – Enabling Robust and Reliable 3-D Interconnect/Integrated Circuit (IC) Technology,” *Procedia Engineering*, vol. 139, pp. 101-111, 2016
[40] M. Holt, R. Harder, R. Winarski and V. Rose, “Nanoscale Hard X-Ray Microscopy Methods for Materials Studies,” *Annual Review of Materials Research*, vol. 43, no. 1, pp. 183-211, 2013
[41] J. Deng, D. J. Vine, S. Chen, Q. Jin, Y. S. G. Nashed, T. Peterka, S. Vogt and C. Jacobsen, “X-ray ptychographic and fluorescence microscopy of frozen-hydrated cells using continuous scanning,” *Scientific Reports*, vol. 7, no. 1, pp. 1-10, 2017
[42] W. S. Drisdell, L. Leppert, C. M. Sutter-Fella, Y. Liang, Y. Li, Q. P. Ngo, L. F. Wan, S. Gul, T. Kroll, D. Sokaras, A. Javey, J. Yano, J. B. Neaton, F. M. Toma, D. Prendergast and I. D. Sharp, “Determining Atomic-Scale Structure and Composition of Organo-Lead Halide Perovskites by Combining High-Resolution X-ray Absorption Spectroscopy and First-Principles Calculations,” *ACS Energy Letters*, vol. 2, no. 5, pp. 1183-1189, 2017
[43] F. Pfeiffer, R. Article and F. Pfeiffer, “X-ray ptychography,” *Nature Photonics*, vol. 12, no. 1, pp. 9-17, 2018
[44] T. W. Victor, L. M. Easthon, M. Ge, K. H. O’Toole, R. J. Smith, X. Huang, H. Yan, K. N. Allen, Y. S. Chu and L. M. Miller, “X-ray Fluorescence Nanotomography of Single Bacteria with a Sub-15 nm Beam,” *Scientific Reports*, vol. 8, no. 1, pp. 1-8, 2018
[45] D. J. Vine, D. Pelliccia, C. Holzner, S. B. Baines, A. Berry, I. McNulty, S. Vogt, A. G. Peele and K. A. Nugent, “Simultaneous X-ray fluorescence and ptychographic microscopy of Cyclotella meneghiniana,” *Optics Express*, vol. 20, no. 16, pp. 18287, 2012
[46] Y. S. Chu, W.-K. Lee, R. Tappero, M. Ge, X. Huang, X. Xiao, H. Yan, P. Northrup, J. Thieme, A. M. Kiss, G. J. Williams, Y. Yang, S. L. Nicholas, A. Pattammattel, R. Smith, P. Ilinski and Y. Du, “Multimodal,

Multidimensional, and Multiscale X-ray Imaging at the National Synchrotron Light Source II," *Synchrotron Radiation News*, vol. 33, no. 3, pp. 29-36, 2020

[47] T. Link, S. Zabler, A. Epishin, A. Haibel, M. Bansal and X. Thibault, "Synchrotron tomography of porosity in single-crystal nickel-base superalloys," *Materials Science and Engineering: A*, vol. 425, no. 1-2, pp. 47-54, 2006

[48] L. Helfen, T. Baumbach, P. Mikulík, D. Kiel, P. Pernot, P. Cloetens and J. Baruchel, "High-resolution three-dimensional imaging of flat objects by synchrotron-radiation computed laminography," *Applied Physics Letters*, vol. 86, no. 7, pp. 071915, 2005

[49] L. Helfen, A. Myagotin, A. Rack, P. Pernot, P. Mikulík, M. Di Michiel and T. Baumbach, "Synchrotron-radiation computed laminography for high-resolution three-dimensional imaging of flat devices," *physica status solidi (a)*, vol. 204, no. 8, pp. 2760-2765, 2007

[50] L. P. Hunter, "Direct measurement of the angular dependence of the imaginary part of the atomic scattering factor of germanium," *IBM Journal of Research and Development*, vol. 3, no. 2, pp. 106-113, 1959

[51] N. W. M. Ritchie, "Efficient Simulation of Secondary Fluorescence Via NIST DTSA-II Monte Carlo.," *Microsc Microanal*, vol. 23, no. 3, pp. 618-633, 2017

[52] A. G. Karydas, "Self-element secondary fluorescence enhancement in XRF analysis," *X-Ray Spectrometry*, vol. 34, no. 5, pp. 426-431, 2005

[53] A. Shajkofci and M. Liebling, "Spatially-Variant CNN-Based Point Spread Function Estimation for Blind Deconvolution and Depth Estimation in Optical Microscopy," *IEEE Transactions on Image Processing*, vol. 29, pp. 5848-5861, 2020

[54] M. Weigert, U. Schmidt, T. Boothe, A. Müller, A. Dibrov, A. Jain, B. Wilhelm, D. Schmidt, C. Broaddus, S. Culley, M. Rocha-Martins, F. Segovia-Miranda, C. Norden, R. Henriques, M. Zerial, M. Solimena, J. Rink, P. Tomancak, L. Royer, F. Jug and E. W. Myers, "Content-aware image restoration: pushing the limits of fluorescence microscopy.," *Nat Methods*, vol. 15, no. 12, pp. 1090-1097, 2018

[55] D. He, D. Cai, J. Zhou, J. Luo and S.-L. Chen, "Restoration of Out-of-Focus Fluorescence Microscopy Images Using Learning-Based Depth-Variant Deconvolution," *IEEE Photonics Journal*, vol. 12, no. 2, pp. 1-13, 2020

Supporting Information:

# Accounting for Sample Morphology in Correlative X-Ray Microscopy via Ray Tracing

Rishi E. Kumar, Xueying L. Quinn, David P. Fenning
Materials Science and Engineering
University of California, San Diego

## Sample preparation and Characterization

The full details on Eu:$CsPbBr_3$ sample fabrication and characterization procedures can be found in Quinn *et al* [1].

## Ray-Tracing Detailed Methods

### *Constructing a 3D Model of Sample Morphology*

Ray tracing of probe-sample interactions requires a 3D model of the sample. We generate this model of our microcrystal by extrusion of measured profilometry data (Figure S1a-b). First, we mask the raw profile to isolate the crystal data from the background data. Next, we fit a plane to the background signal and subtract this from the raw profile. Finally, we construct a 3D binary array with dimensions matching that of the crystal profile, where indices at or below the $z$ value measured at that $(x,y)$ coordinate in the profile are set to *True*. This approach assumes that there are no voids or overhangs below the measured profile - for samples where this assumption is not valid, a different approach can be employed. The goal of this step is to build a 3D mask of the sample extent, and the ray tracing itself is agnostic to how this mask is constructed.

### *Defining the Measurement Geometry and Simulation Mesh*

The instrument geometry is defined with respect to sample plane by the Euler angles of the incident beam and the detector axis. For the sake of simplicity in our specific case, we rotated our simulation volume such that these directions are contained within the $xz$ plane, allowing us to fully describe the geometry with two angles. (Figure S1c). Our synchrotron measurements utilized a nanoprobe with a beam waist of <200 nm. As such, we treat both the incident probe and signal photons as pencil beams propagating directly along the directions defined by these two angles.

The mesh for the ray tracing simulation is defined by the 3D sample mask and the instrument geometry. We first interpolated the sample mask onto a mesh scaled to match the highest resolution dimension (in our case, the z-dimension), effectively generating more points along the coarse lateral dimensions. This mesh is extended along the $x$-dimension to accommodate for the lateral projection of the beam trajectory by $x_{extension} = z_{max}\cos(\theta_{incident})$.

### *Approximating Attenuation Within the Sample*

To calculate attenuation of incident and collected photons within the sample, we must know the X-ray attenuation coefficient within our sample for relevant photon energies. First, we define the density and nominal elemental composition of our material. From this the number density ($mol/cm^3$) of each atomic species is computed, and the attenuation coefficient is approximated as the weighted average of the individual elements' atomic scattering factors.[2]

### *Ray Tracing*

For each lateral coordinate $(x, y)$ a single ray is simulated starting from the top of the simulation mesh $(x, y, z_{max})$. As this ray propagates along the incident direction with a step size $d_{step}$, two events occur for each step where the ray intersects the sample: the intersection is recorded, and a signal ray is spawned. The signal ray similarly propagates towards the detector until $z = z_{max}$, and the total number of steps where the sample is intersected is recorded. These processes, formalized in algorithms (1) and (2), repeat until the incident ray reaches $z = 0$, and repeat for each lateral coordinate $(x, y)$. A schematic of one ray simulation is shown in Figure 1g.

Note that the simulation to this point has been purely geometric, yielding a table of intersection points for measurement at each lateral coordinate of the sample. Once the incident and detected photons energies $E_{incident}, E_{signal}$ are defined, the attenuation coefficients $\mu_{incident}, \mu_{signal}$ are estimated as described above. These coefficients are applied to the tabulated intersection points from ray tracing results. Attenuation of these photons at each intersection point is calculated as $A = 1 - e^{-\mu d_{step}}$ according to Beer-Lambert's law. This overall process is formalized in algorithm (3). The total signal measured at each lateral coordinate $(x, y)$ is taken to be the sum of all final signal ray intensities at that coordinate. By separating the expensive ray tracing from the attenuation calculations, we quickly apply the ray tracing results to fluorescence data for elements with different emission energies.

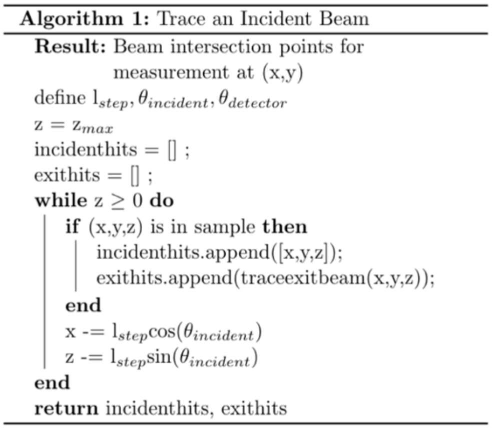

**Algorithm 1:** Trace an Incident Beam

```
Result: Beam intersection points for
        measurement at (x,y)
define $l_{step}, \theta_{incident}, \theta_{detector}$
$z = z_{max}$
incidenthits = [] ;
exithits = [] ;
while $z \geq 0$ do
    if (x,y,z) is in sample then
        incidenthits.append([x,y,z]);
        exithits.append(traceexitbeam(x,y,z));
    end
    x -= $l_{step}\cos(\theta_{incident})$
    z -= $l_{step}\sin(\theta_{incident})$
end
return incidenthits, exithits
```

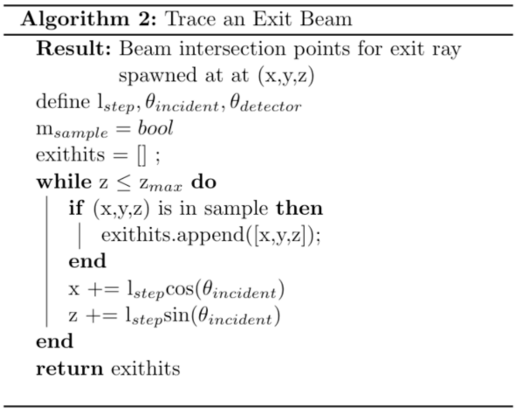

**Algorithm 2:** Trace an Exit Beam

```
Result: Beam intersection points for exit ray
        spawned at at (x,y,z)
define $l_{step}, \theta_{incident}, \theta_{detector}$
$m_{sample} = bool$
exithits = [] ;
while $z \leq z_{max}$ do
    if (x,y,z) is in sample then
        exithits.append([x,y,z]);
    end
    x += $l_{step}\cos(\theta_{incident})$
    z += $l_{step}\sin(\theta_{incident})$
end
return exithits
```

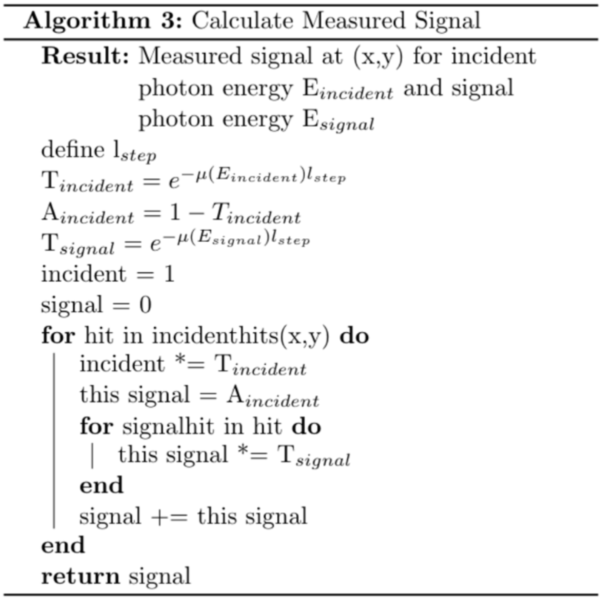

**Algorithm 3:** Calculate Measured Signal

```
Result: Measured signal at (x,y) for incident
        photon energy $E_{incident}$ and signal
        photon energy $E_{signal}$
define $l_{step}$
$T_{incident} = e^{-\mu(E_{incident})l_{step}}$
$A_{incident} = 1 - T_{incident}$
$T_{signal} = e^{-\mu(E_{signal})l_{step}}$
incident = 1
signal = 0
for hit in incidenthits(x,y) do
    incident *= $T_{incident}$
    this signal = $A_{incident}$
    for signalhit in hit do
        this signal *= $T_{signal}$
    end
    signal += this signal
end
return signal
```

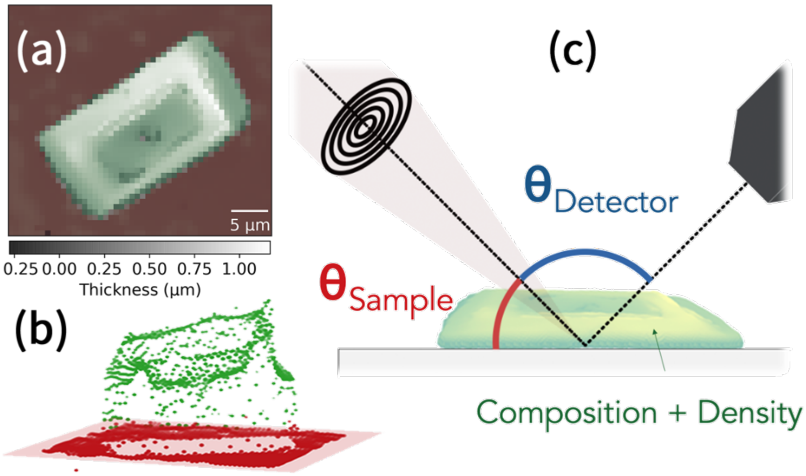

Figure S1: (a) Profilometry data of our isolated Eu:CsPbBr$_3$ crystal. False coloring indicates sample (green) and background (red) regions. (b) The surface profile of the crystal (green) after removal of the background baseline (red). (c) Three-dimensional solid body model of the crystal formed by extrusion of the green points, along with the material properties and measurement geometry parameters required to define the ray-tracing simulation.

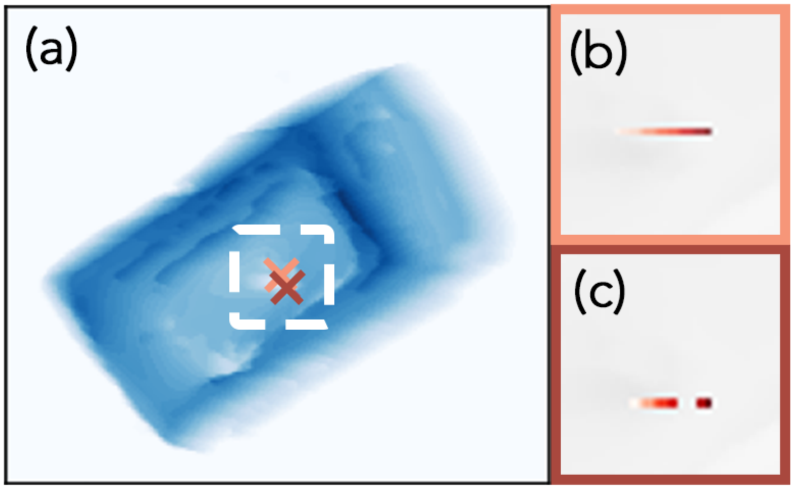

Figure S2: Local sample point-spread function (sPSF) for two points on the sample, marked in (a), are shown in (b) and (c).

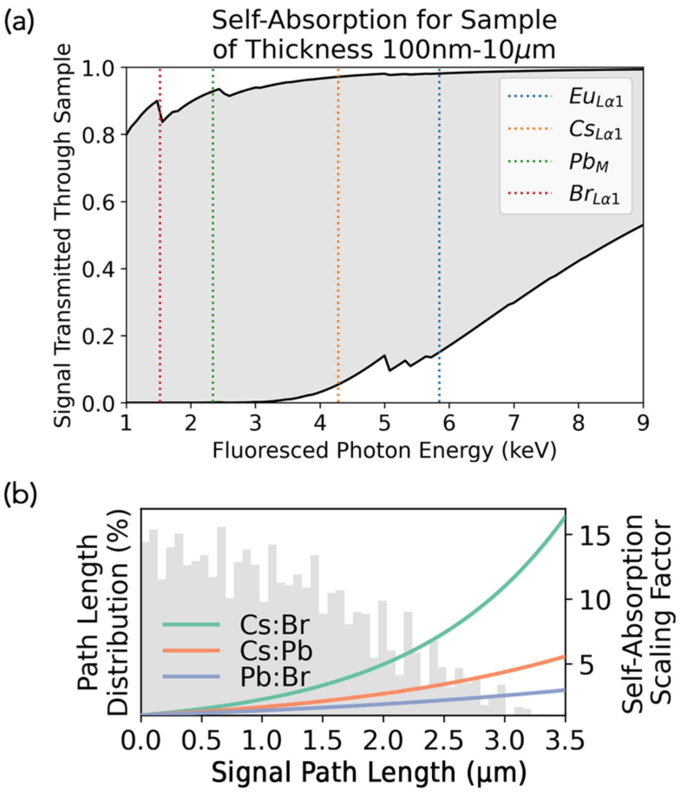

Figure S3: (a) The fraction of fluorescence signal transmitted through our perovskite sample to the detector for optical path lengths ranging from 0.1 to 10 μm. Emission energies for the four elements of interest in our sample are indicated. (b) A histogram of fluorescence signal path lengths as recorded from ray tracing in the nXRF geometry. The three overlaying traces indicate the degree to which molar ratios between majority elemental species in our sample are skewed in the raw fluorescence data as a function of signal path length.

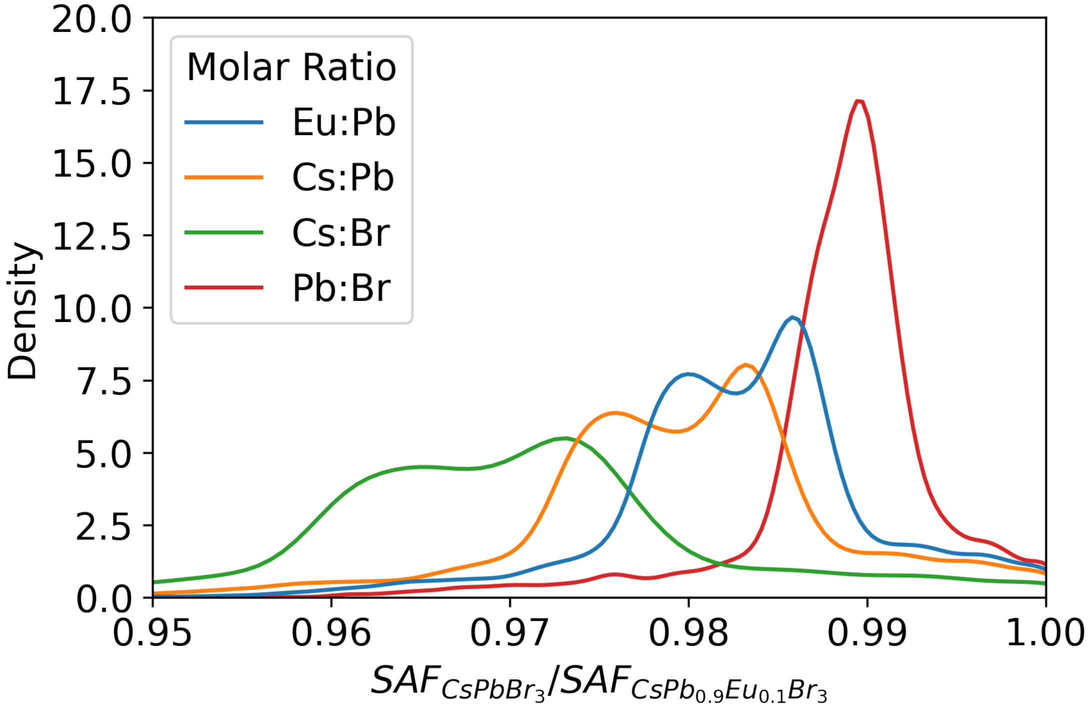

Figure S4: Effect of sample composition on molar ratios after self-absorption correction for points across the sample area. The compositions are selected as the extreme ends of compositional variation based on measured composition. The distribution of values results from the variation in path lengths across the sample.

**References**

[1] X. L. Quinn, R. E. Kumar, M. Kodur, D. N. Cakan, Z. Cai, T. Zhou, M. V. Holt and D. P. Fenning, Adv. Optical Mater. 2002221 (2021). 10.1002/adom.202002221
[2] B. L. Henke, E. M. Gullikson and J. C. Davis, Atomic data and nuclear data tables. **54**, 181-342 (1993).